Supporting Information

Resolving the non-Arrhenius behavior of Oxygen Anion Conductivity in YSZ Using Off-Lattice and Coarse-Grained Kinetic Monte Carlo

Yi-Wen Wei[1], Shu-Hui Guan[1], Cheng Shang[1], Zhi-Pan Liu[1,2]*

[1]Collaborative Innovation Center of Chemistry for Energy Material, Shanghai Key Laboratory of Molecular Catalysis and Innovative Materials, Key Laboratory of Computational Physical Science, Department of Chemistry, Fudan University, Shanghai 200433, China

[2]State Key Laboratory of Metal Organic Chemistry, Shanghai Institute of Organic Chemistry, Chinese Academy of Sciences, Shanghai 200032, China

TABLE OF CONTENTS

1. Exponential Fit of the min-E_a Distribution

To quantify the statistical distribution of IS escape difficulty, we define min-E_a for each IS as the smallest activation barrier among all outgoing elementary reactions and plot its probability density P(min-E_a) (i.e., the normalized histogram of min-E_a over all ISs) together with an exponential fit in Figure S1; it shows an excellent exponential decay (R^2 = 0.99), with the configuration density dropping by ~646 from 0.1 to 0.7 eV.

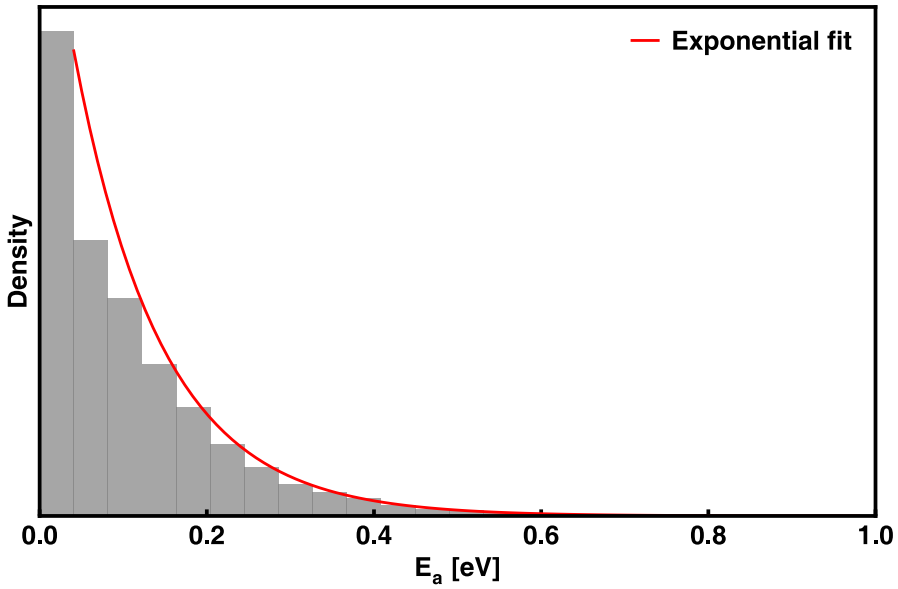

Figure S1. Exponential fit of min-E_a for all ISs.

2. Inverse Correlation Between Escape Rate $\widetilde{R}$ and min-E_a

To explore the relationship between the temperature-dependent escape rate $\widetilde{R}$ and the escape barrier, we compute $\widetilde{R}$ for each IS at 800 K (Eq. 4) and plot its correlation with min-E_a in Figure S2; it shows a clear inverse correlation (Pearson's r = −0.72), indicating faster escape from low-barrier ISs and slower escape from high-barrier ISs.

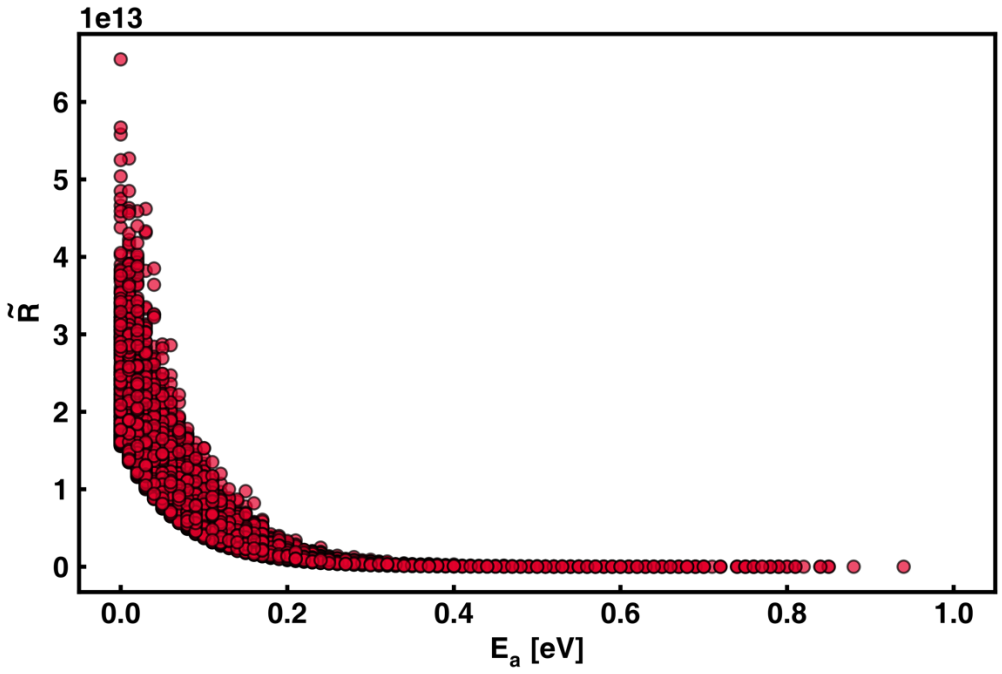

Figure S2. Pearson Correlation Scatter Plot

3. GM Structure and Symmetry-Equivalent O_v Sites

To document the GM structure adopted from our previous work, we plot the GM configuration and its symmetry-equivalent vacancy sites in Figure S3; it shows a 1×2×2 supercell built from a 79-atom conventional unit cell (27 cations) with four Zr^{4+} substituted by Y^{3+} (Y1–Y4), creating two chemically distinct O_v (V1 and V2). For both V1 and V2, the first-nearest cation neighbors are all Zr^{4+}, while the second-nearest cation shell contains three Y dopants (V1: Y1, Y3, and Y4; V2: Y2, Y3, and Y4). Each vacancy type has four symmetry-equivalent sites in the 1×2×2 supercell, yielding eight O_v in the GM configuration.

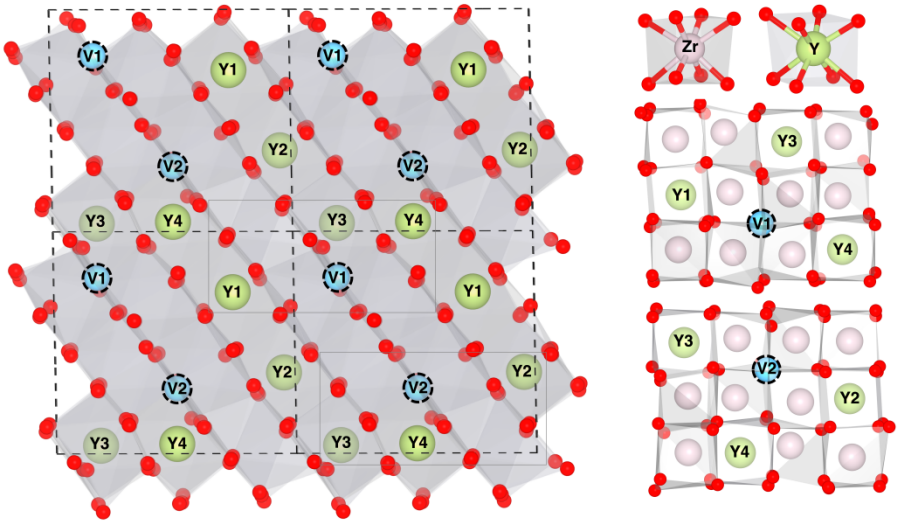

Figure S3. Atomic structures of GM.

4. Homogeneous O_v–O_v Distance Distributions for All Eight Vacancies in the GM

To confirm whether oxygen vacancies are uniformly arranged in the GM, we compute the O_v–O_v distance distribution using each of the eight vacancies as the reference (O_v-1 to O_v-8) and plot the resulting curves in Figure S4; it shows that all curves have the same peak positions (dominant nearest-neighbor peak at ~5.8 Å, followed by weaker peaks at ~8.9 and ~9.7–10 Å), indicating that all vacancies share an equivalent local environment and thus form a homogeneous O_v distribution in the GM.

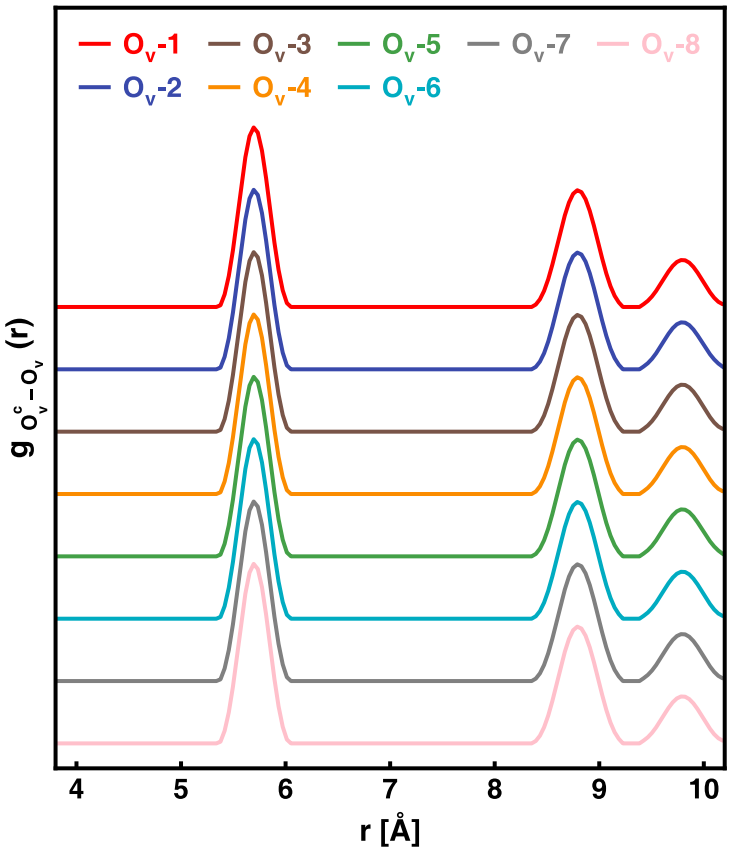

Figure S4. RDFs g(r) of the O_v^m-O_v pairs, where O_v^m represents the selected O_v in GM.

5. Library-Size Convergence of CG-KMC Diffusivity

The central approximation of CG-KMC is to replace the explicit microscopic evolution on the high-energy network with a finite set of pre-recorded GM-to-GM excursions, while reproducing the D. In a production CG-KMC simulation, the system propagates between successive visits to the GM by repeatedly sampling excursions from a library containing N_{lib} distinct trajectories. Each executed excursion r contributes a net displacement increment and an associated time increment. After executing excursions, the cumulative displacement and elapsed time are

$$R = \sum_{r=1}^{N_{run}} \Delta R_r$$

$$t = \sum_{r=1}^{N_{run}} \Delta t_r$$

from which D are evaluated via Eq. 10. Increasing the library size N_{lib} improves the representation of the underlying GM-to-GM excursion ensemble and reduces the systematic bias, leading to convergent conductivity once N_{lib} is sufficiently large. To test convergence with respect to the GM-to-GM excursion library size, we run four CG-KMC simulations at 800 K with N_{lib} = 30, 50, 100, and 137 distinct GM-to-GM trajectories, and plot D as a function of N_{lib} in Figure S5; it shows that D is essentially converged for $N_{lib} \geq 50$.

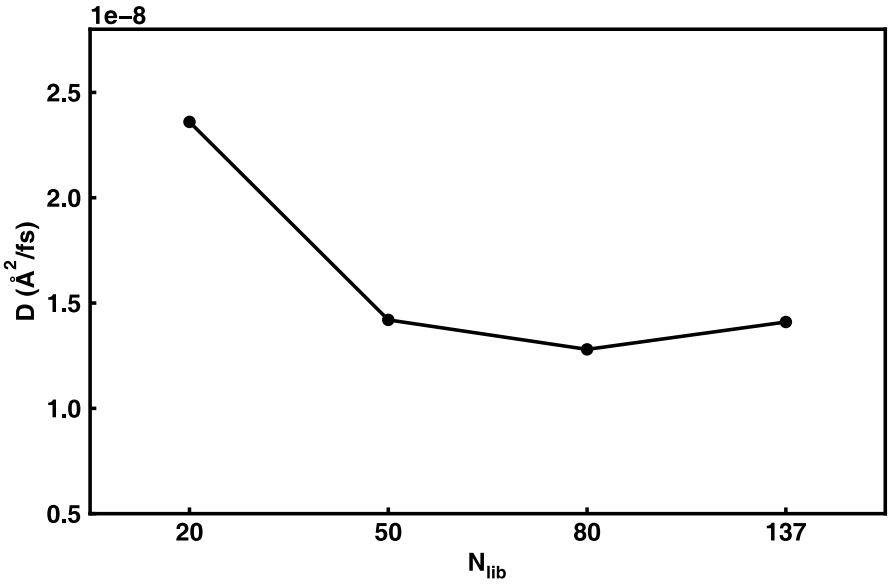

Figure S5. D-N_{lib} plot at 800 K.

6. Time Convergence of CG-KMC Diffusivity

To demonstrate that KMC reaches converged long-time diffusion at low temperatures, we plot the time evolution of the diffusivity D(t) from the 800 K KMC trajectory in Figure S5, and overlay the plateau value D_∞ (defined as the mean over the final 10% of the trajectory) together with a ±5% convergence band; it shows that D(t) approaches D_∞ and remains within the ±5% band by the end of the 0.04 ms simulation window.

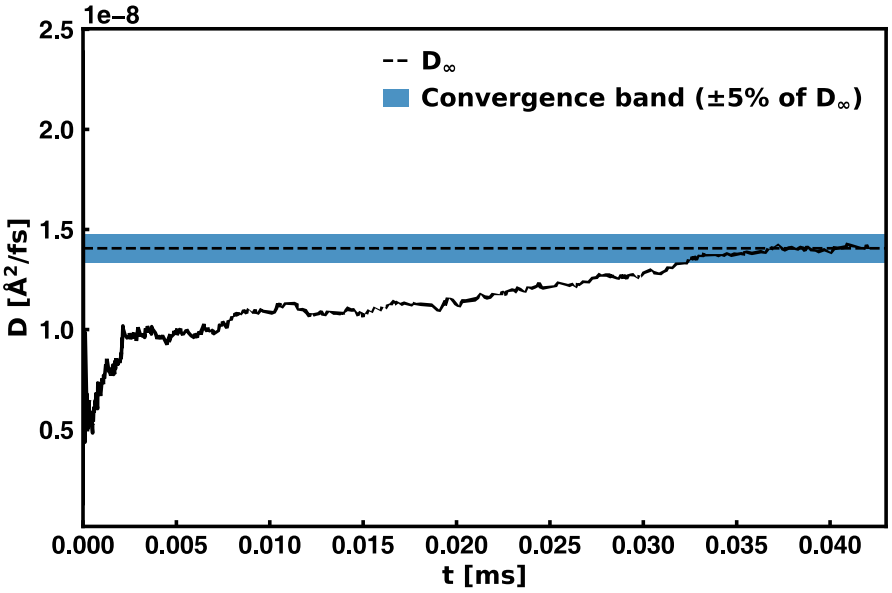

Figure S6. D–t plot at 800 K.

7. Temperature Dependence of the Immediate Return Probability to the GM Basin

Once the system resides in a non–GM local minimum, a direct re-entry into the GM basin can only occur from a subset of non-GM minima that are kinetically adjacent to the GM. In our network construction, this subset H is taken as 200 FSs appearing in the GM Path. For each m ∈ H, we quantify its equilibrium contribution within the non-GM ensemble by the Boltzmann weight fraction

$$f_m = \frac{\exp^{-\beta E_m}}{\sum_{m\neq GM}^{n} \exp^{-\beta E_m}};\ \beta = \frac{1}{k_B T}$$

where E_m is the energy of configuration m and the denominator is the total equilibrium weight of all non-GM configurations included in the network. Conditioned on the system being in configuration m, the probability that the next KMC event returns directly to the GM basin is defined as the branching probability

$$P_{m\to GM} = \frac{k_{m\to GM}}{\tilde{R}_m}$$

where $k_{m\to GM}$ is the transition rate from i into the GM basin. The return probability is then

$$P_{r-GM} = \sum_{m\in H} f_m\, P_{m\to GM}$$

The resulting P_{r-GM} as a function of temperature is shown in Figure S7. It shows that P_{r-GM} increases monotonically with temperature from ~0.7% at 800 K to ~3.3% and then saturates above ~1600 K.

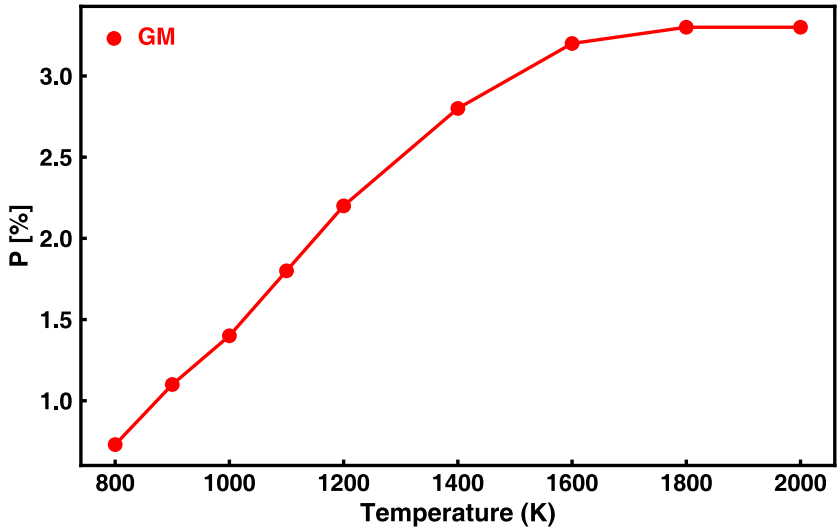

Figure S6. P_{r-GM} over 800-2000 K.

8. Thermal Expansion Effect on a Key GM Escape Barrier

To evaluate the effect of thermal expansion on the key migration barrier, we obtained equilibrium lattice parameters at 800 and 1600 K from NPT molecular dynamics simulations. These temperature-dependent cell parameters were then used to re-optimize the corresponding GM structures under the expanded lattices. Based on these structures, the barrier of a key GM escape event was recalculated. As summarized in Table S1, the barriers are 1.16, 1.14, and 1.18 eV at 0, 800, and 1600 K, respectively. The small variation indicates that the key barrier depends only weakly on lattice parameter, supporting the applicability of the static-lattice rate list over a broad temperature range.

Table S1. Cell volumes and calculated barriers of a key GM escape event (GM→ Str4) at 0, 800, and 1600 K

Temperature (K)	Volume (Å^3)	E_a (eV)
0	3832.68	1.16
800	3953.22	1.14
1600	4056.96	1.18

9. Upper Bound of the No-Return Overestimation Factor (Γ_{max}) Across Temperature

To bound the conductivity overestimation introduced by the no-return policy, we define an upper-limit factor $\Gamma_{max} = 1/p_{GM}$ from the equilibrium occupation probabilities and tabulate Γ_{max} as a function of temperature in Table S2; it shows that Γ_{max} is essentially unity at low temperatures (≤1000 K, 1.00–1.01) but increases at high temperatures (1.41 at 1600 K to 2.70 at 2000 K), indicating that the no-return error is negligible in the low-temperature regime where p_{GM} dominates.

Table S2. Γ_{max} at 800-2000 K

Temperature	Γ_{max}
800	1.00
900	1.01
1000	1.01
1100	1.03
1200	1.06
1400	1.17
1600	1.41
1800	1.87
2000	2.70